Segmentation of Neck Lymph Nodes in CT Datasets with Stable 3D Mass-Spring Models

Abstract

The quantitative assessment of neck lymph nodes in the context of malignant tumors requires an efficient segmentation technique for lymph nodes in tomographic 3D datasets. We present a Stable 3D Mass-Spring Model for lymph node segmentation in CT datasets. For the first time, our model concurrently represents the characteristic gray value range, directed contour information as well as shape knowledge, which leads to a robust and efficient segmentation process. Our model design and the segmentation accuracy were both evaluated with 40 lymph nodes from 5 clinical CT datasets containing malignant tumors of the neck. The segmentation accuracy proved to be comparable to those of manual segmentations by experienced users and significantly reduced the time and interaction needed for the lymph node segmentation.

Key words: Segmentation, Deformable Models, Lymph Nodes, Stable Mass-Spring Models

1 Motivation

The assessment of lymph nodes plays an important role in the diagnosis, staging, treatment and therapy control of malignant tumors and their metastases. MRI and CT scans of the respective regions often allow for a 3D assessment of the pathological situation. For surgery and radiation planning as well as for therapy control, an exact quantitative analysis of the lymph nodes' volume, growth, their infiltration of and distance to neighboring structures are essential. This demands a segmentation of the lymph nodes from the 3D datasets.

Lymph node segmentation currently often has to be performed manually by delineation of the contour in all involved slices of the 3D dataset. This may take up to 20 minutes per dataset, when many enlarged lymph nodes are contained [1]. This effort makes an accurate quantitative lymph node evaluation often unfeasible in the time-critical clinical routine. We present an efficient model-based segmentation technique for enlarged lymph nodes (1 cm – 3 cm) in CT datasets of the neck, which significantly reduces the time and the interaction effort for lymph node segmentation.

Automatic segmentation of neck lymph nodes is a difficult task, due to the various anatomical situations lymph nodes may occur in (Fig. 1), leading to four main problems:

- Neck lymph nodes often touch or infiltrate adjacent soft tissue (Fig. 1 (b), (c)), which lets all pure gray value-based segmentation techiques fail.
- Adjacent high-contrast structures often lead to high gradient magnitudes in the local neighborhood (Fig. 1 (d)), which may distract model-based segmentation approaches based on contour strength.
- The lymph nodes' interior homogeneity may be disturbed by a central necrosis (Fig. 1 (e)).
- The size of metastatic lymph nodes varies significantly.

(a) (b) (c) (d) (e)

Fig. 1. Different anatomical situations in CT head and neck data: (a) isolated neck lymph node, (b) neck lymph node adjacent to M. sternocleidomastoideus, (c) two adjacent lymph nodes, (d) lymph node touching high-contrast structure (blood vessel), (e) lymph node with a central necrosis (dark).

2 State of the Art

The segmentation of lymph nodes in CT image data has long been known as an open problem. Rogowska et al. [2] evaluated elementary segmentation techniques (e.g., Thresholding, Watershed Transformation, etc.) for lymph node segmentation, and conclude that a high degree of model knowledge is needed for a reliable segmentation.

Honea et al. [3] used a slicewise two-dimensional Active Contour as a first model-based segmentation approach. The adapted contour of each slice is propagated to the neighboring slice for initialization. This approach was extended by using a 3D Active Contour model [4]. Both their 2D and 3D approach are purely based on contour information (gradient magnitude) and shape knowledge (represented by a viscosity condition).

Yan et al. [5] exploited the characteristic gray value range as well as the contour information of lymph nodes by using an improved 2D Fast Marching Method with an intensity-weighted speed term. However, no shape knowledge was used by their approach. Boundary leaking could only be avoided by a hard stopping criterion (the user places a bounding circle around the lymph node).

Both the approaches of Yan and Honea require high interaction effort. No quantitative evaluation with clinical CT datasets was performed. No approach integrates all characteristic features of the lymph nodes: contour information, characteristic gray value range and shape knowledge.

In a more recent publication, Unal et al. [6] used an implicit shape model to register an ellipse to lymph nodes in LN-MRI images. The 2D ellipse concurrently evolves in the T2 and T2* images and is then propagated to the next slices in 3D.

Besides lymph node segmentation techniques, newer approaches are known on the segmentation of small homogeneous soft tissue structures in CT data (e.g., pulmonary nodules [7]). However, these approaches presume a homogeneous background, which makes them inappropriate for the segmentation of neck lymph nodes in their complex anatomical environment.

Several techniques are known that use prior shape knowledge for the segmentation process. This shape knowledge can be represented by a curvature constraint or smoothness condition as in the work of Honea and Cohen [8], and Delingette's Simplex Meshes [9]. In other publications, more specific shape knowledge is often integrated by coupling a deformable segmentation model with a point distribution model [10]. Except for Honea's work mentioned above, none of these techniques have been applied to lymph node segmentation yet. In fact, our work shows that the simple ellipsoidal character of lymph nodes can be sufficiently modelled by a curvature constraint, without the need for using a more sophisticated point distribution model.

3 Method

We employ Stable 3D Mass-Spring Models (SMSMs) introduced by Dornheim et. al. [11] for the neck lymph nodes segmentation, which shall be shortly introduced:

3.1 Stable 3D Mass-Spring Models

Mass-Spring Models (MSMs) are physically-based models known from soft tissue simulation. They use *spring forces* to describe the object shape by the distance of connected mass points. MSMs can also be applied as deformable models for segmentation. In this case, no simulation of a real physical situation is required. Instead, the model dynamics is used to adapt a deformable shape to image information by a local optimization process. This process is

comparable to the adaptation of an Active Contour Model—it aims at finding an equilibrium between the internal forces describing the model's shape, and external forces describing the image information. For this purpose, however, the representation of shape only by spring forces is not stable enough and often leads to model shape collapse, especially in 3D (see Figure 2 (a)).

SMSMs extend conventional MSMs by not only incorporating the springs' *rest lengths,* but also their *rest directions*. Whenever a spring deviates from its rest direction, a *torsion force* is created to restore its original direction (see Figure 2 (b), (c)). Thus, the object shape is mainly represented by the springs' rest directions, while their rest lengths represent the object's scaling.

Fig. 2. Torsion Forces: (a) Shape collapse due to a sensor force, (b) rest directions of two springs, (c) torsion forces restore the deviated springs' rest directions

The external model forces of an SMSM are created by *sensors* at the mass points. They transform the image information at their current position into a *sensor force* acting on the associated mass point. For the segmentation of lymph nodes, two types of sensors are of interest: *intensity sensors*, dragging their associated mass to voxels of a given gray value range, and direction-weighted *gradient sensors*, steering towards voxels at gradients of high magnitude and preferable expected direction.

For three major reasons, we chose to use an SMSM for the lymph node segmentation:

- Stable 3D Mass Spring Models can easily be created from a sample segmentation [12]. This allows a fast and flexible model creation which is appropriate for lymph nodes, which have a very simple shape with little characteristic shape variability.
- The volumetric sampling of the dataset by mass points allows to represent contour and gray value information concurrently in the model.
- The separation of the model's size and its shape by the use of spring and torsion forces allows to represent the lymph nodes' shape, while leaving the size of the target lymph nodes flexible.

3.2 Design of the Lymph Node Model

The manual segmentation of lymph nodes exploits a set of characteristic features, which all together allow the human observer to detect lymph nodes in CT datasets. The following features were derived from lymph nodes in 25 clinical CT datasets of the neck containing malignant tumors with lymph node dissemination:

(i) Ellipsoidal to spherical shape with a varying ratio of longitudinal and transversal radii. This ratio is approximately 2:1 for healthy lymph nodes. With metastatic lymph nodes, it approaches 1:1.
(ii) Medium strength of contour information for isolated lymph nodes. Contours of non-isolated lymph nodes can be interrupted by adjacent soft tissue or amplified by adjacent high-contrast structures.
(iii) Homogeneous gray value (soft tissue) in the lymph node interior (with the exception of lymph nodes with a central necrosis).
(iv) Size varies strongly: neck lymph nodes are clinically relevant at a size of 1 cm, the maximum size can be assumed as 3 cm, since larger lymph nodes must be considered as "real" metastases, which are often not spherical.

To model the ellipsoidal to spherical shape of the lymph nodes (i), a 3D SMSM was created as a polygonic sphere surface (Fig. 3 (a)). At each mass point, a direction-weighted gradient sensor was placed in order to model the contour information (ii) including the local contour normal direction that we expect to find here. The sensor force created from the gradient sensor is projected to the normal direction at its associated mass. This makes the model adaptation more target-directed and stable. The required normal direction of each mass is computed as the average normal of all its adjacent faces, weighted by the incident angle.

To incorporate the additional knowledge about the inner gray value of the lymph nodes (iii) into the model, we created a second, inner sphere surface (Fig. 3 (b)) as a downscaled copy (scaling factor 0.9) of the first surface. At each mass point of this inner surface, an intensity sensor was placed, searching for the specific gray value of the target lymph node. We chose to arrange these inner sensors as another surface, instead of distributing them evenly across the lymph node interior, in order to segment lymph nodes with inner necrosis.

In a final modelling step, each gradient sensor of the outer surface was connected to its associated intensity sensor at the inner surface (Fig. 3 (c)). To make both associated sensors work as a functional unit, we assigned all springs between the two surfaces a very high stiffness (factor 1000 to all other springs) (Fig. 3 (d)). This way, each intensity sensor keeps its associated gradient sensor close to the homogeneous lymph node interior and prevents model distraction

by false strong gradients (ii). All other springs, i.e., the springs belonging to one of the surface submodels, were assigned a very low stiffness, in order to represent the unknown size of the lymph nodes (iv). In connection with the shape-preserving torsion forces, model shape stability is guaranteed [11] and can be expected to bridge gaps in the lymph node contour (ii) by shape knowledge.

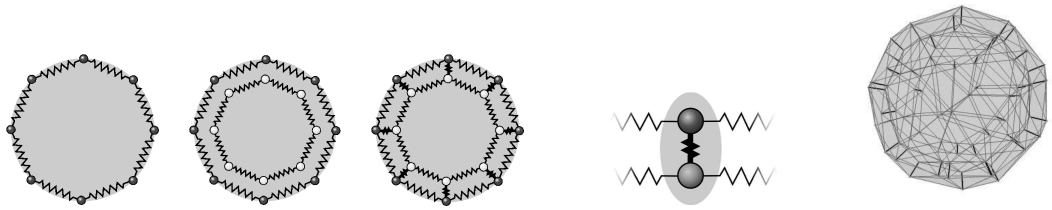

Fig. 3. Stages of the model construction (schematic 2D view): (a) First surface model with gradient sensors (dark gray). (b) An inner front of intensity sensors (white) is added. (c) Both fronts are connected by stiff springs, the associated gradient and intensity sensor act as a functional unit (d), (e): the complete 3D model.

3.3 Segmentation Process

Once the model has been created as described above, the segmentation of a given lymph node consists of the following three steps:

Step 1: Initial placement of the model in the dataset.

Since the model simulation is based on a local optimization process [11], the model should initially be placed inside the homogeneous interior of the target lymph node. Thereto, the user specifies a seed point, at which a scaled model of minimal size (0.3mm) is placed automatically, assuming that all lymph nodes are at least twice as large as this minimal size ("1-point initialization", Figure 4 (a)).

Alternatively, the initial model can be specified by two seed points at the lymph node's contour. Their distance is used as the intial model's diameter ("2-points initialization", Figure 4 (b)). This more precise initialization leads to faster model convergence. After model initialization, the rest lengths of all springs are set to their current lengths, so that the new model size is its default size.

(a) (b)

Fig. 4. Initial placement of the model by (a) 1-point initialization and (b) 2-points initialization

Step 2: Automatic determination of gray value range.

The gray value range of different lymph nodes may vary slightly, even within the same dataset. Therefore, we estimate the target lymph node's expected gray value range from the given start position. Thereto, the average gray value G of all voxels inside the sphere is calculated. The model's intensity sensors are then programmed to only react to gray values inside the interval $[G - g_{min}\,;\, G + g_{max}]$. The values of $gmin$ and $gmax$ have been determined once by experimental model runs for all lymph nodes (see Table 1).

Step 3: Model adaptation.

Finally, the model adaptation is run (Figure 5) with the runtime parameters shown in Table 1. They were adjusted once by experimental model runs and then used for all datasets during the evaluation phase.

To automate the segmentation process as far as possible, we determine when the model adaptation has come to a rest. The model adaptation is automatically stopped when every mass point remains inside a certain ε environment for n simulation steps. Due to the use of a damping force, the model always converges and stops.

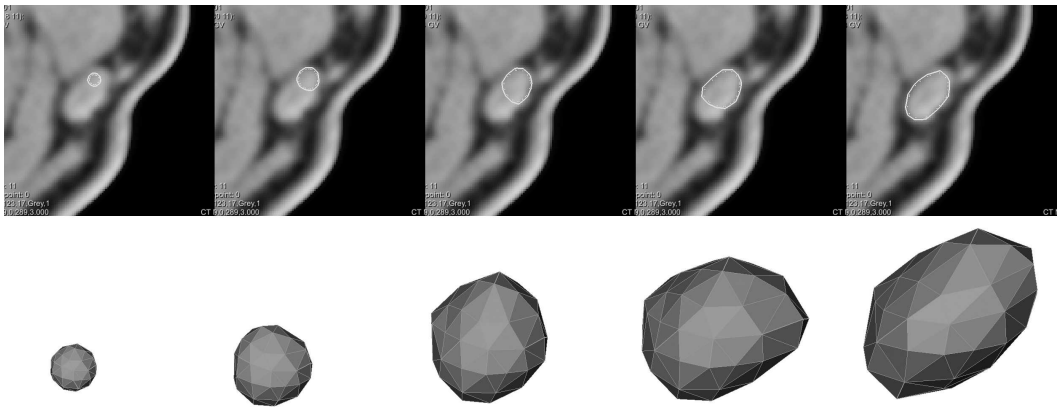

Fig. 5. 2D and 3D view of the model adaptation process.

4 Results and Evaluation

We carried out three studies to verify our method. First, a qualitative study was performed to validate the model design, and to reveal which components of the model were most important for good segmentation results. Afterwards, a quantitative evaluation of the segmentation accuracy was performed. Finally, we assessed the robustness of our method with respect to the user's initial placement of the model.

11 CT datasets of the neck region with 146 enlarged lymph nodes were available for the evaluation. The datasets stem from different CT devices, the quality of the datasets varied significantly with respect to signal-to-noise ratio, horizontal resolution and slice distance (see Table 2).

For 40 lymph nodes in 5 of the 11 datasets, a gold standard (segmentation by a radiologist) was given, as well as manual segmentations by two experienced users. All evaluation was performed with the created SMSM (100 masses, 338 springs), without manual correction of the results.

Table 1
Model simulation parameters (according to [11])

Parameter Category	Parameter Description	Symbol	Value
Model adaptation	Simulation step size	$\triangle t$	0.02
	Tolerance (stopping criterion)	ε	0.01 mm
	Simulation steps (stopping criterion)	n	5
Weighting of force components	Torsion forces	w_t	25
	Spring forces	w_f	20
	Gradient sensor forces	w_{s_g}	9
	Intensity sensor forces	w_{s_i}	6
Constants for model elements	Torsion constant	T_{ij}	1
	Spring stiffness (surface)	S_{ij}	0.01
	Spring stiffness (functional unit)	S_{ij}	10
	Mass	m_i	1
Gray value range	Lower interval margin	g_{min}	150 HU
	Upper interval margin	g_{max}	100 HU

4.1 Qualitative Evaluation of the Model Design

We first performed a qualitative study to validate the model design and to reveal, which components of the model are essential. Thereto, we started the model simulation with different model components disabled on specific lymph nodes of the 11 test datasets. The following results could be verified.

Shape stability due to torsion forces.

The torsion forces proved to be suitable for the representation of the shape knowledge. We first tested this behaviour with lymph nodes touching high-contrast structures. The shape stability gained by the use of torsion forces prevents the model from being distracted by the strong gradients of these neighboring structures (Fig. 6 (a) and (b)). In cases with lymph nodes adjacent to soft tissue structures, the torsion forces caused the model to extrapolate the organic lymph node surface by shape knowledge at places with weak or missing contour information (Fig. 6 (c) and (d)).

Table 2
Datasets used for the evaluation

	Dataset Size		Voxel Size		Miscellaneous			
#	X/Y	Z	X/Y	Z	Slice thickness	Contrast agent	Device	Lymph Nodes
1	512	65	0.28	3	3 mm	yes	Siemens	26
2	512	61	0.28	3	3 mm	yes	Siemens	5
3	512	26	0.41	1.95	2 mm	no	Siemens	10
4	512	61	0.45	3	3 mm	no	Siemens	10
5	512	42	0.44	5	5 mm	yes	Siemens	6
6	512	63	0.42	3	3 mm	yes	GE	15
7	512	262	0.47	0.7	1 mm	yes	Philips	17
8	512	229	0.51	0.51	1 mm	yes	Siemens	5
9	512	31	0.53	3	3 mm	no	Siemens	6
10	512	161	0.41	1.5	3 mm	yes	Philips	35
11	512	52	0.35	3.9	4 mm	yes	PI, Inc.	11

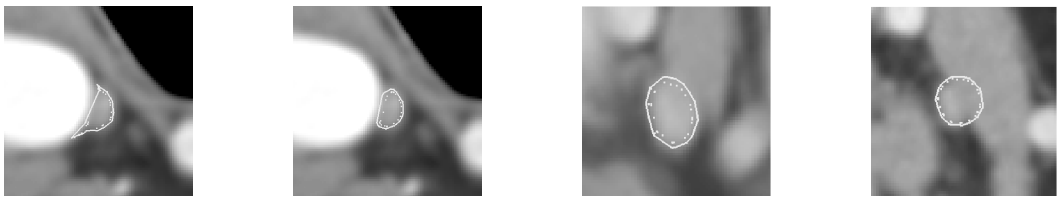

(a) (b) (c) (d)

Fig. 6. Effect of the torsion forces on the segmentation results: (a) distraction of gradient sensors by stronger neighboring gradients. In (b), this distraction is prevented by the shape-stabilizing effect of the torsion forces. In (c) and (d), the shape knowledge of the model extrapolates missing contour information, where the lymph node touches the adjacent muscle.

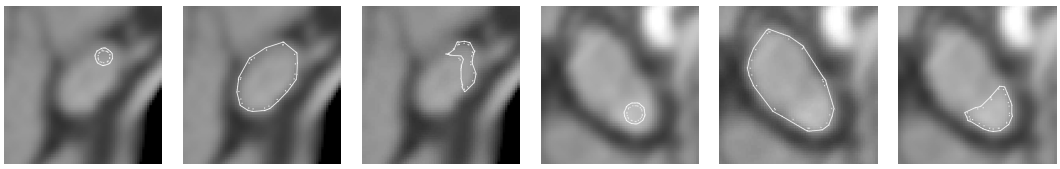

(a) (b) (c) (d) (e) (f)

Fig. 7. Effect of the torsion forces on the size adaptation of the model: (a), (d): initial model placement, (b), (e): adaptation with active torsion forces, (c), (f): model degeneration with inactive torsion forces

Adaptation to lymph node size.

Our model proved to be able to adapt to lymph nodes of different sizes, even with imprecise initial positioning. We verified this behavior with 8 isolated lymph nodes and a very small model initialization. The segmentation process was started once with active and once with inactive torsion forces. The model adapted completely to the size of the target lymph node in all cases with active torsion forces (Figure 7). Without torsion forces, the model degenerated in 5 of 8 cases. This shows that the flexible size adaptation of the model is made possible by the torsion forces, which are characteristic for the used deformable model. The flexible size adaptability is essential for the application of lymph nodes segmentation, as we do not know in advance how large a target lymph node is.

Functional unit of gradient and intensity sensors.

The combination of intensity and gradient sensors turned out to be essential for the successful segmentation. We verified this with 10 lymph nodes adjacent to high-contrast structures. Without intensity sensors, the strong neighboring gradients often attracted single gradient sensors, which lead to "leaking" into the high-contrast structure (Fig. 8 (a)). In cases of small lymph nodes, often the whole model adapted to the complete shape of the blood vessel (Fig. 8

(c)). With the combined use of gradient and intensity sensors, this behavior was completely eliminated.

The results of our qualitative analysis show that only the combination of all above-described model components—shape knowledge, gray value and gradient information—enables a robust lymph node segmentation.

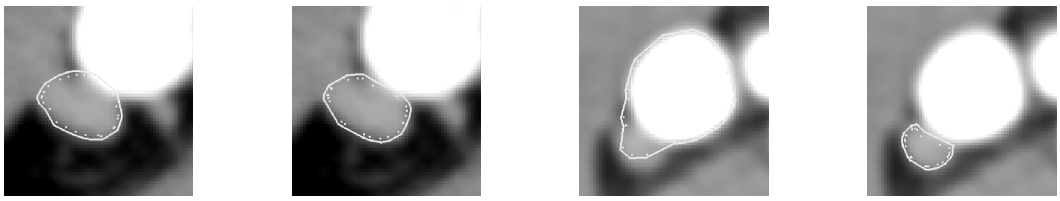

(a) (b) (c) (d)

Fig. 8. Segmentation results with gradient sensors only (a, c), and with combined gradient and intensity sensors (b, d).

4.2 Quantitative Evaluation of Segmentation Accuracy

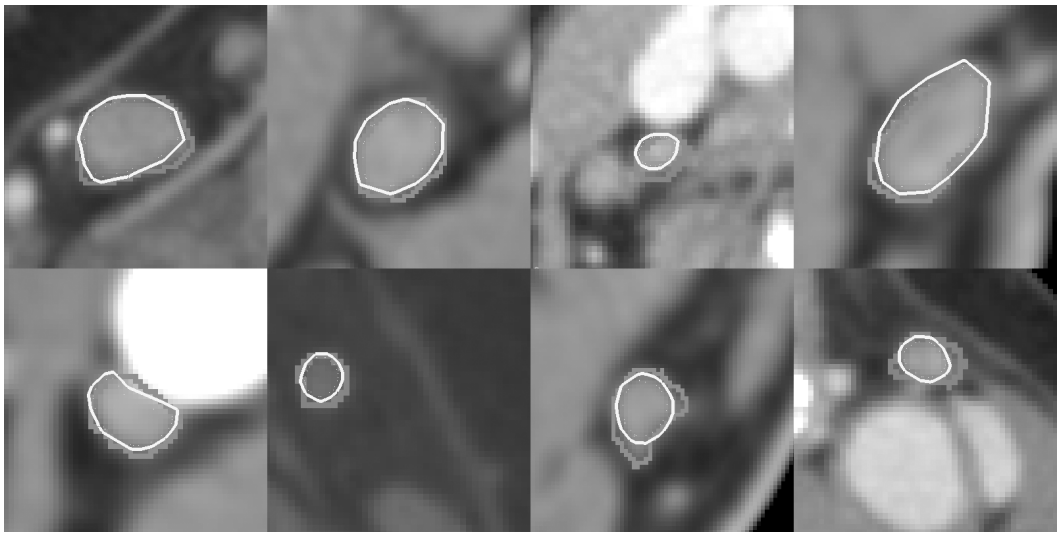

Fig. 9. Segmentation results of the lymph node model (white) and gold standard segmentation (light gray)

To evaluate the accuracy of our model-based segmentation, we assembled a quantitative analysis based on the 40 lymph nodes for which a gold standard was available. These 40 lymph nodes represent all problem classes of homogeneous lymph nodes (see Fig. 1 (a)–(d): isolated lymph nodes, weak gradient, strong gradient, deformed lymph nodes). They were equally distributed across 5 of the 11 CT neck datasets.

We used the 2-points initialization to place the model in each of the 40 lymph nodes and started the model simulation with the parameters given in Table

Table 3
Results of the quantitative evaluation

	Dataset	1	2	3	4	5
Mean	User A	0.420	0.353	0.401	0.311	0.296
Surface	User B	0.488	0.406	0.444	0.271	0.279
Distance (mm)	Model	0.421	0.309	0.596	0.583	0.416
Hausdorff	User A	3.513	2.401	3.238	1.213	1.575
Distance	User B	4.113	2.644	3.225	1.150	1.725
(mm)	Model	3.913	2.350	3.825	1.700	1.925
Volumetric	User A	45.88	69.38	43.25	35.13	37.00
Segmentation	User B	45.63	65.25	50.88	29.88	33.13
Error (%)	Model	44.38	50.75	51.38	51.75	38.88

1. After 2 to 30 seconds, the model simulation stopped automatically for all 40 lymph nodes on a modern standard PC (3.2 GHz Pentium 4). The model's segmentation result, as well as the manual expert segmentations for all 40 lymph nodes were then compared to the given gold standard (see Fig. 9 and Table 3 for results). Our analysis showed that the accuracy of our segmentation model is comparable with the accuracy of the given manual segmentations.

The mean surface distance of the model's segmentation results varied between 0.3 mm and 0.6 mm, while the Hausdorff distance varied between 1.7 mm and a maximum of 3.9 mm. For the Hausdorff distance, the biggest errors stem from different estimations of the upper and lower border of the lymph node, which is directly correlated with the slice distance (up to 3.9 mm). Since this deviation could also be observed for manual segmentations, it shows that this is still a general problem, which can only be reduced by smaller slice distances.

4.3 Robustness of the Method

In order to assess the robustness of the SMSM-based lymph node segmentation, we examined its dependency from the given seed point. The placement of the model inside a lymph node is well-defined for smaller lymph nodes, which do not leave much space for strongly differing placements of the segmentation model. For small lymph nodes, the segmentation accuracy is therefore easily reproducible.

In contrast to that, with larger lymph nodes, the user has much more freedom to place the model in different positions, which makes their reproducible seg-

mentation potentially problematic. To examine this dependency on strongly varying initial placements, we selected the 10 largest out of the 40 lymph nodes for which a gold standard was available.

For each of the 10 lymph nodes we placed 5 different seed points into the lymph node's interior. The first seed point was placed visually in the center of the lymph node. Two seed points were placed in the same slice as the center, along the longest diameter, halfway between the center and the lymph node border. The last two seed points are placed on the longest diameter in z direction, also halfway between the lymph node's center and its border. For each seed point in each of the 10 lymph nodes, we started the segmentation process and compared the segmentation result with the gold standard.

The results for all 10 lymph nodes are shown in Figure 10. It can be seen that 4 out of 10 large lymph nodes showed varying segmentation results. In all other cases, the variation of the model's segmentation results was comparable to the variations of manual segmentations by the two expert users (the average standard deviation of the mean surface distance (mm) to the gold standard was 0.05).

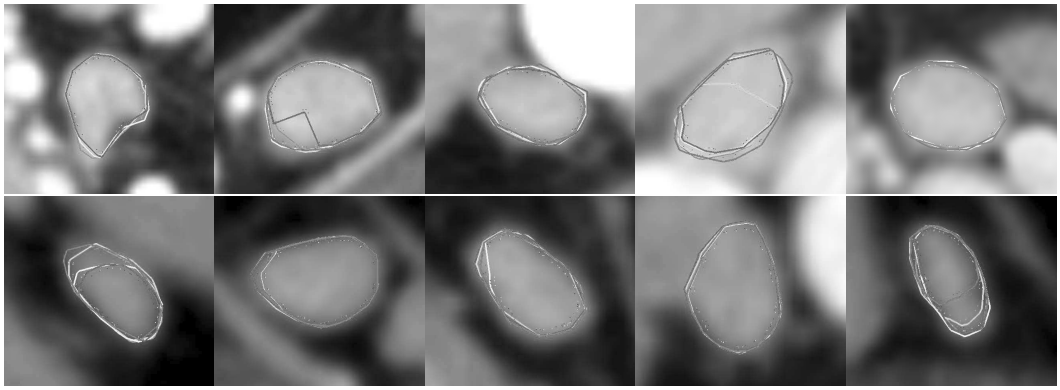

Fig. 10. Segmentation results for the 10 largest lymph nodes, each with five different seed points

Figure 11 shows the distribution of lymph node sizes across the 40 lymph nodes with a gold standard. 75% are small lymph nodes for which model placement is not problematic. Therefore, for 90% of our 40 lymph nodes the segmentation accuracy does not depend on the initial model placement. The problematic 10 % are all large lymph nodes.

Quantitative analysis of these results revealed that the segmentation accuracy variation results from different stable states that the model can reach on these lymph nodes. For large lymph nodes, the homogeneity condition of our model is sometimes interrupted. Such slight inhomogeneities can result from a beginning central necrosis leading to additional gradients in a lymph node's interior. In other cases, large lymph nodes are actually a conglobation of adjacent smaller lymph nodes, which have grown into each other. In these

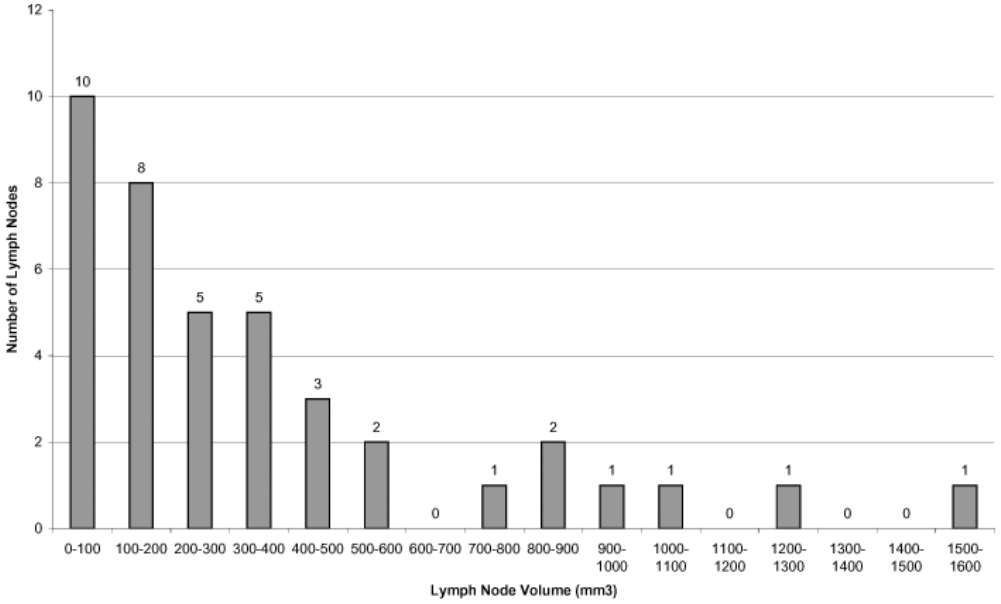

Fig. 11. Distribution of lymph node sizes across the 40 test lymph nodes

cases, there are also very small gradients in the lymph nodes' interior, thus, our model only segments some of the lymph nodes.

5 Conclusion

We presented a new 3D segmentation technique for lymph nodes in CT datasets, using deformable models (SMSMs). For the first time, this allowed to incorporate the three characteristic features of lymph nodes—gray value range, contour information and shape knowledge—into one single 3D model. This results in a robust and efficient segmentation process with minimal interaction needed.

The presented technique was evaluated with 40 lymph nodes from clinical CT datasets and could be proved to be comparable to the manual segmentation results of two experienced users. Our qualitative analysis showed that all elements of our model design were indeed essential for the successful segmentation. In additional tests, our model proved to be robust to the initial placement, which makes its results well reproducable.

The time and interaction effort needed for lymph node segmentation is reduced significantly by our technique, which is a precondition for its integration into the preoperative surgery planning.

Future work includes the integration of our segmentation technique in an ap-

propriate user interface, which allows for a large-scale evaluation in a clinical setting. Due to their local parameterization and their physical behavior, we expect mass-spring models to be well suited for applying local interactive corrections intuitively. This is an advantage with respect to correction of segmentation errors, and an interaction of the user during the model run is also possible.

Currently, the described segmentation approach has not been applied to lymph nodes with a central necrosis. An adaptation to this special type of lymph nodes is intended. Further work will also aim at automatic lymph node detection leading to a set of starting points, which can then be used to segment the detected lymph nodes with our method. The robustness of our method with respect to the 1-point placement will be advantegeous for that.

References

[1] J. Cordes, J. Dornheim, B. Preim, I. Hertel, G. Strauß, Preoperative segmentation of neck ct datasets for the planning of neck dissections, in: Proc. SPIE Medical Imaging 2006: Image Processing, 2006.

[2] J. Rogowska, K. Batchelder, G. Gazelle, E. Halpern, W. Connor, G. Wolf, Evaluation of selected two-dimensional segmentation techniques for computed tomography quantification of lymph nodes, in: Investigative Radiology, Vol. 13, 1996, pp. 138–145.

[3] D. M. Honea, Y. Ge, W. E. Snyder, P. F. Hemler, D. J. Vining, Lymph node segmentation using active contours, in: Proc. SPIE Medical Imaging 1997: Image Processing, Vol. 3034, 1997, pp. 265–273.

[4] D. Honea, W. E. Snyder, Three-dimensional active surface approach to lymph node segmentation., in: Proc. SPIE Medical Imaging 1999: Image Processing, Vol. 3361, 1999, pp. 1003–1011.

[5] J. Yan, T. ge Zhuang, B. Zhao, L. H. Schwartz, Lymph node segmentation from CT images using fast marching method, Computerized Medical Imaging and Graphics 28 (2004) 33–38.

[6] G. Unal, G. Slabaugh, A. Ess, A. Yezzi, T. Fang, J. Tyan, M. Requardt, R. Krieg, R. Seethamraju, M. Harisinghani, R. Weissleder, Semi-automatic lymph node segmentation in ln-mri, in: Proc. of ICIP (International Conference on Image Processing), 2006.

[7] J.-M. Kuhnigk, V. Dicken, L. Bornemann, D. Wormanns, S. Krass, H.-O. Peitgen, Fast automated segmentation and reproducible volumetry of pulmonary metastases in CT-scans for therapy monitoring, in: Medical Image Computing and Computer-Assisted Intervention – MICCAI 2004, Vol. 3217, 2004, pp. 933–941.

[8] C. L. Cohen, I., N. Ayache, Using deformable surfaces to segment 3d images and infer differential structures, CVGIP: Image Understanding 56 (2) (1992) 242–263.

[9] H. Delingette, Adaptive and deformable models based on simplexmeshes, in: IEEE Workshop of Non-Rigid and Articulated Objects, 1994.

[10] J. Montagnat, H. Delingette, Volumetric medical images segmentation using shape constrained deformable models, in: CVRMed, 1997, pp. 13–22.

[11] L. Dornheim, K. Tönnies, J. Dornheim, Stable dynamic 3d shape models, in: International Conference on Image Processing (ICIP), 2005.

[12] L. Dornheim, J. Dornheim, T. K.D., Automatic generation of dynamic 3d models for medical segmentation tasks, in: SPIE Medical Imaging 2006, 2006.